Theor Chem Acc (2010) 127:467–474
DOI 10.1007/s00214-010-0734-6

REGULAR ARTICLE

Electronic structures and spectroscopic properties of promising highly efficient red phosphorescent Os(II)$(LR)_2(PH_3)_2$ complexes: a theoretical exploration

Jian-Po Zhang · Bao-Hui Xia · Li Jin · Hong-Xing Zhang

Received: 1 January 2010 / Accepted: 5 February 2010 / Published online: 4 March 2010

Abstract The red phosphorescent osmium(II) complexes $[Os(LR)_2(PH_3)_2]$ (L = 2-pyridyltriazole (ptz): R = H (**1a**), CF_3 (**1b**), *t*-Bu (**1c**)); L = 2-pyridylpyrazole (ppz): R = H (**2a**), CF_3 (**2b**), *t*-Bu (**2c**)); L = 2-phenylpyridine (ppy): R = H (**3a**)) were explored using density functional theory (DFT) methods. The ground- and excited-state geometries of the complexes were optimized at the B3LYP/LANL2DZ and UB3LYP/LANL2DZ levels, respectively. The absorption and phosphorescence of the complexes in CH_2Cl_2 media were calculated based on the optimized ground- and excited-state geometries using time-dependent density functional theory method with the polarized continuum model. The optimized geometry structural parameters of the complexes in the ground state agree well with the corresponding experimental values. The lower-lying unoccupied molecular orbitals of the complexes are dominantly localized on the L ligand, while the higher-lying occupied ones are composed of Os(II) atom and L ligand. The low-lying metal-to-ligand and intraligand charge transfer (MLCT/ILCT) transitions and high-lying ILCT transitions are red-shifted with the increase in the π-donating ability of the L ligand and the π electron-donating ability of R substituent. The calculation revealed that the phosphorescence originated from ^{3}MLCT/^{3}ILCT excited state. However, the complex **3a** displayed different types of MLCT/ILCT excited state compared with that of **1a**–**2c**, and the different types of transition were also found in the absorption. In addition, we found that the phosphorescence quantum efficiency of Os(II) complexes is related to the metal composition in the high-energy occupied molecular orbitals, it will be helpful to designing highly efficient phosphorescent materials.

Keywords Osmium(II) complexes · Electronic structures · Spectroscopic properties · TD-DFT calculations · UB3LYP methods

1 Introduction

Phosphorescent transition-metal complexes with d^6 electronic configuration has been extensively investigated experimentally and theoretically in the last decades [1, 2]. These complexes have been applied as highly efficient electroluminescent (EL) emitters in various potential fields including organic lightemitting devices (OLEDs) [3], biological labeling reagents [4], photocatalysts for CO_2 reduction [5, 6], as well as catalysts [7]. Most of the above characters of the d^6 metal complexes are ascribed to the imposed strong spin–orbit coupling effect of the metal atom, which can effectively promote singlet-to-triplet intersystem crossing and enhance the consequent radiative

Electronic supplementary material The online version of this article (doi:10.1007/s00214-010-0734-6) contains supplementary material, which is available to authorized users.

J.-P. Zhang · B.-H. Xia · H.-X. Zhang (✉)
State Key Laboratory of Theoretical and Computational Chemistry, Institute of Theoretical Chemistry, Jilin University, 130023 Changchun
People's Republic of China
e-mail: zhanghx@mail.jlu.edu.cn; canoe8013@126.com

B.-H. Xia
College of Chemistry, Jilin University, 130023 Changchun, People's Republic of China

J.-P. Zhang · L. Jin
School of Chemical and Pharmaceutical Engineering, Jilin Institute of Chemical Technology, 132022 Jilin, People's Republic of China

transition from the triplet state to the single state. Thus, in theory, an internal phosphorescence quantum efficiency (η_{int}) could achieved as high as 100% [8].

In the past years, attentions were once focused on Ir(III) and Pt(II) complexes, such as $[Ir(ppy)_3]$ (ppy = 2-phenylpyridine), $[Pt(trpy)C \equiv CR]^+$ (trpy = 2,2′,6′,2″-terpyridine) [9, 10], because they hold a large number of fascinating photochemical properties such as UV/Vis absorption, photoluminescence, and long-lived emission. In comparison, although much less explored, Os(II) complexes may gain certain advantages, such as the reduction of radiative lifetime and hence, a possibility of higher luminescent efficiency, over the traditional Ir(III) and Pt(II) emitting materials in OLED applications. So, several research groups have paid much attention to the Os(II) complexes, a lot of complexes such as $[Os(bpy)_3]^{2+}$, $[Os(trpy)_2]^{2+}$, and $[Os(CO)_3X((acac)R_1R_2)]$ (acac = acetoylacetonate; X = halides or tfa, tfa = trifluoroacetate; R_1 or R_2 = -CF_3, -C_6H_5, -$C_{10}H_7$) [11–13] have been synthesized, and their spectral properties have been investigated both experimentally and theoretically. The results show that these complexes exhibit high quantum efficiencies and long radiative lifetime; the phosphorescence can be predominantly described as originating from three types of triplet excited states from the metal-to-ligand charge transfer (^{3}MLCT) transition, ligand-to-ligand charge transfer (^{3}LLCT) transition, and intraligand charge transfer (^{3}ILCT) transition. Furthermore, the phosphorescence color and transition character can be tuned by changing the ligand and adding electron-withdrawing and electron-donating groups on the ligands. Therefore, the Os(II) complexes can be used as an excellent emitting materials in OLEDs.

Recently, much attention has been paid to the preparation of this class of emissive materials with various types of ligands and to gain more understanding on their associated photophysical properties aimed at applications as OLEDs. Several $[Os(II)(L_1R)_2(L_2)_2]$ complexes (L_1 = 2-pyridyltriazole or 2-pyridylpyrazole; R = CF_3 or t-Bu, and L_2 = PPh_2Me or $PPhMe_2$) have been synthesized experimentally by Chou et al. [14, 15]. The C-linked 2-pyridylazoles show strong acidity, which is reinforced if the attached R ligand displays electron-withdrawing character such as CF_3, then the azoles will readily lose a proton from the NH fragment and produce the stable anionic ligands. The research indicated that the lowest-lying absorption is from a mixing of MLCT and ILCT transition for these red-emitting Os(II) complexes. Based on the small variation of the emission peak wavelengths, they found that the triazolate segment exhibited only a small amount of hypsochromic displacement, although its π-accepting character should be greater than that of the pyrazolate analog. The phosphorescence lifetimes of ca. 0.6–0.9 μs in degassed CH_2Cl_2 for these Os(II) complexes are considerably shorter than those of most reported red-emitting Ir(III) complexes [16], implying that the OLED devices fabricated with these Os(II) complexes could exhibit reduced triplet–triplet annihilation at higher driving voltages [17]. However, there is no theoretical report on the relationship between the geometries and the spectroscopic properties of this new kind of Os(II) complex.

At present, quantum chemistry methods are advanced and efficient enough to explore the electronic properties of transition-metal complexes [18–22]. It is possible to perform systematic theoretical studies on the electronic structures and spectroscopic properties of metal complexes. To understand the similarities and differences in the chemical properties of Os(II) metal complexes with different ligand and substituent, we theoretically investigated the ground and excited states of a series of $[Os(LR)_2(PH_3)_2]$ (L = ptz, ppz, or ppy; R = H, CF_3, or t-Bu) complexes. The important relationship between the quantum efficiencies and the metal composition in the HOMO was revealed.

2 Computational methods

In this work, *Ci* symmetry was adopted to set the conformation of these complexes in both the ground and the excited states. The coordination axis is displayed in the Fig. 1. To save computational resources, in the calculations, we use the PH_3 group to replace the PPh_2Me or $PPhMe_2$ groups appearing in the real molecules [14, 15] due to that the phenyl can hardly influence the spectral properties. Indeed, this kind of simplification has been successfully applied in many works such as using hydrogen to replace methyl, phenyl, and cyclohexyl, heavy substituents [21–24].

Time-dependent density functional theory (TD-DFT) has gained widespread use in photochemistry due to its reasonable accuracy and low computational cost. This method has successfully been used in the excited-states calculations for a variety of molecular systems [25]. The geometric structures in the ground state and lowest energy triplet state were fully optimized at the B3LYP [26] and unrestricted B3LYP (UB3LYP) levels, respectively. On the basis of the optimized ground- and excited-states geometries, the absorption and emission properties in CH_2Cl_2 media were calculated by TD-DFT [27] associated with the polarized continuum model (PCM) [28].

In the calculations, quasirelativistic pseudopotentials of the Os and P atoms proposed by Hay and Wadt [29] with 16 and 5 valence electrons were employed, and a "double-ξ" quality LANL2DZ basis sets associated with the pseudopotential were adopted. A relative effective core

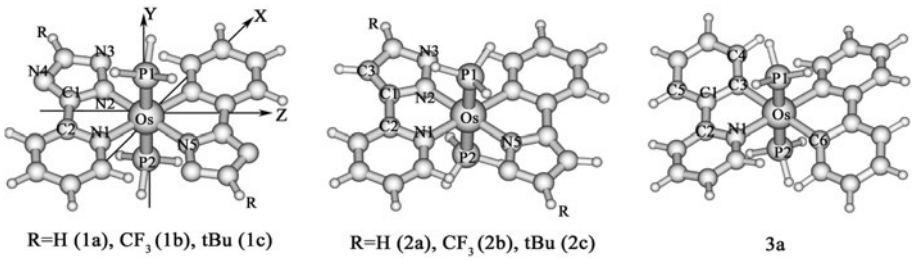

Fig. 1 Structures of [Os(LR)2(PH3)2] (L = 2-pyridyltriazole (ptz): R = H(**1a**), CF3(**1b**), t-Bu(**1c**)); L = 2-pyridylpyrazole (ppz): R = H(**2a**), CF3(**2b**), t-Bu(**2c**)); L = 2-phenylpyridine (ppy): R = H (**3a**))

potential (ECP) on Os replaces the inner core electrons leaving the outer core $[(5s^2)(5p^6)]$ electrons and the $(5d^6)$ valence electrons for Os(II). In addition, to describe the molecular properties precisely, one f-type and one d-type polarization function ($\alpha_f = 0.886$, $\alpha_d = 0.34$) were augmented to the Os(II) and P atoms. The basis sets were described as Os (8s6p3d1f/3s3p2d1f), P(3s3p1d/2s2p1d), C, N, F(10s5p/3s2p), and H (4s/2s). All the calculations are accomplished using the Gaussian03 (Revision C.02) program package [30] on an origin/3900 server.

3 Results and discussion

3.1 Ground-state geometries and the frontier molecular orbital properties

The main optimized geometry structural parameters in the ground state together with the X-ray crystal diffraction data of **2b** are given in Table 1, and the optimized geometries are shown in Fig. 1. The optimized bond lengths and bond angles of **2b** in the ground state are in general agreement with the corresponding experimental values [14, 15]. The calculated bond lengths of Os–P1 (2.360 Å), Os–N1 (2.115 Å), Os–N2 (2.075 Å), and N2–N3 (1.352 Å) of **2b** are ca. 0.002, 0.025, 0.002, and 0.003 Å in comparison with the measured values. In addition, the bond angles and dihedral angles are also reproduced. The bond angles of N1–Os–N2 and N1–Os–N5 are 76.5° and 103.5°, which is in full agreement with their experimental values. The bond lengths and bond angles of the other complexes are similar to those of **2b**. The dihedral angle of N1–Os–N2–N3 is about 179.9° for **1a–2c,** which indicates that the two chelating pyridylazoles ligands establish a nearly planar OsN_4 basal arrangement. The planar ligand arrangement is analogous to those of the porphinato ligand in metalloporphyrins such as $[Os(ttp)(PPh_3)_2]$ (ttp = meso-tetraphenylporphinate) [31]. But, for **3a,** the ppy ligand and Os atom do not share the same plane as indicated by its dihedral angle of N1–Os–C3–C4 (166.2°). The discrepancy of the geometry structural is reasonable and acceptable, since the strong interaction among the ppy, PH_3 ligands, and Os atom and results in the twist of ppy plane.

The compositions of the frontier molecular orbital of **1a–3a** are given in Table 2 and S-Tables 1–6 (Supporting Information), and the energy level diagrams of the frontier molecular orbital are given in Fig. 2. Table 2 and S-Tables 1–6 show that the π^*-type molecular orbitals are mainly composed of L ligand with more than 90.0% composition, while the first three high-energy occupied orbitals are dominantly contributed by d(Os) and a spot of π(L), which are hardly affected by changing the L ligand and R substituent. This case is similar to the Ir(III) analogs $[trans\text{-}(C\hat{}N)_2Ir(PH_3)_2]^+$ [32], except that there are more metal compositions of Os(II) complexes (>50%) in the high-energy occupied MOs.

From Fig. 2, it is very obvious that the HOMO and LUMO energy level of **1a–3a** show a regular change with

Table 1 Optimized geometry parameters of **1a–3a** for the ground states, together with the experimental values of **2b** from X-ray diffraction

	Os–P1	Os–N1	Os–N2	N2–N3	N1–Os–N2/C3	N1–Os–N5/C6	N1–Os–N2/C3–N3/C4
1a	2.347	2.115	2.071	1.375	76.8	103.2	179.9
1b	2.363	2.121	2.071	1.367	76.7	103.3	179.8
1c	2.355	2.119	2.076	1.373	76.6	103.4	179.8
2a	2.352	2.121	2.081	1.361	76.6	103.4	179.9
2b	2.360	2.115	2.075	1.352	76.5	103.5	179.9
Exp[a]	2.362	2.090	2.073	1.349	76.5	103.5	
2c	2.351	2.114	2.082	1.360	76.6	103.4	179.8
3a	2.328	2.113			76.9	103.1	166.2

Distances are given in Å, angles and dihedral angles in degree

[a] Experimental results from Refs. [14, 15]

Table 2 Partial molecular orbital contributions (%) of **1a** in the ground state at the B3LYP level

Orbital	Energy (ev)	Composition (%)			Main bond type	Os component
		Os	2ptz	$2PH_3$		
$51a_u$	0.9530	3.2	67.9	28.9	$\pi^*(ptz) + \pi^*(PH_3)$	
$50a_u$	0.7026	14.1	11.6	74.3	$d(Os) + \pi^*(ptz) + \pi^*(PH_3)$	$13.9p_z$
$49a_u$	0.6114	41.8	3.9	54.3	$d(Os) + \pi^*(PH_3)$	$40.9p_z$
$48a_u$	0.5353	22.5	10.8	66.7	$d(Os) + \pi^*(ptz) + \pi^*(PH_3)$	$22.19p_z$
$49a_g$	0.4770	34.8	9.7	55.5	$d(Os) + \pi^*(ptz) + \pi^*(PH_3)$	$11.3d_{x^2-y^2} + 6.7d_{z^2} + 15.9s$
$48a_g$	−0.8163	1.8	97.0	1.2	$\pi^*(ptz)$	
$47a_u$	−0.9415	2.7	93.2	4.0	$\pi^*(ptz)$	
$47a_g$	−1.2691	8.2	91.3	0.6	$\pi^*(ptz)$	
$46a_u$	−1.7734	2.9	91.2	5.9	$\pi^*(ptz)$	
HOMO-LUMO energy gap						
$46a_g$	−5.0913	61.1	34.0	4.9	$d(Os) + \pi(ptz)$	$48.7d_{xy} + 11.9d_{yz}$
$45a_g$	−5.3060	79.8	19.8	0.4	$d(Os) + \pi(ptz)$	$28.6d_{xz} + 23.6d_{x^2-y^2} + 23.3d_{z^2}$
$44a_g$	−5.6638	69.6	24.9	5.5	$d(Os) + \pi(ptz)$	$53.9\ d_{yz} + 12.3d_{xz}$
$45a_u$	−6.3961	0.2	98.6	1.3	$\pi(ptz)$	
$43a_g$	−6.5904	8.4	90.7	0.9	$\pi(ptz)$	
$44a_u$	−7.2494	0.5	99.4	0.1	$\pi(ptz)$	
$42a_g$	−7.2494	0.4	99.5	0.1	$\pi(ptz)$	
$43a_u$	−7.4228	1.4	69.1	29.5	$\pi(ptz) + \pi(PH_3)$	
$42a_u$	−7.9276	2.6	96.9	0.4	$\pi(ptz)$	
$41a_u$	−8.0522	1.9	78.8	19.4	$\pi(ptz) + \pi(PH_3)$	
$41a_g$	−8.1284	12.8	83.1	4.2	$d(Os) + \pi(ptz)$	

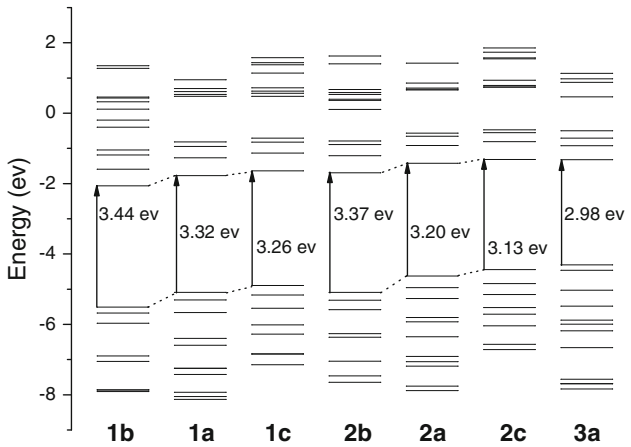

Fig. 2 Energy-level diagrams of frontier molecular orbitals related to the absorptions for all the complexes

the variation of the L ligand and R substituent. It can be noted that, with the enhancement of the π-donating ability of the L ligand in the order **1a** < **2a** < **3a**, the orbital energy of the HOMO and LUMO remarkably increase, while the HOMO-LUMO energy gap decrease. The similar trend was also found at **1a**–**c** and **2a**–**c,** with the increase in the π electron-donating ability of R substituents in the order of **b** < **a** < **c,** the orbital energy of HOMO and LUMO increase, and the HOMO-LUMO energy gap also decrease.

3.2 Absorptions spectra in CH_2Cl_2 media

The calculated absorptions in the UV–vis region and their oscillator strengths, the main configuration, and their assignments are given in Table 3 and S-Tables 7–12 for **1a** and **1b**–**3a**, respectively. The corresponding fitted Gaussian-type absorption curves with the calculated absorption data are shown in Fig. 3, and S-Figs. 1, 2. To intuitively understand the electron transition processes, we depicted the related electron density diagrams in Figs. 4, 5, 6.

As seen in Fig. 3, within the considered energy range, the absorption spectra of **1a**–**3a** show three absorption bands. Table 3 and S-Tables 7–12 show the lowest-lying absorptions of **1a**–**3a** at 494 (2.51), 474 (2.61), 503 (2.47), 512 (2.42), 479 (2.59), 524 (2.37), and 586 nm (2.11 eV), respectively. With respect to **1a**, the excitation of MO $46a_g \rightarrow$ MO $46a_u$ is dominantly responsible for the absorption band at 494 nm. Table 3 shows that MO $46a_g$ is composed of 48.7% d_{xy}(Os) and 34% π(ptz), and in MO $46a_u$, the ptz ligand contributes 91.2% π* type component. Thus, the absorption at 494 nm for **1a** can be assigned to a $[d_{xy}(Os) + \pi(ptz)] \rightarrow [\pi^*(ptz)]$ transition with MLCT and

Table 3 Calculated absorptions of **1a** in the CH_2Cl_2 solution at the TD-DFT (B3LYP) level

States	Transition	|CI Coef.| >0.3	E, nm (ev)	Oscillator	Assignment
^1A_u	$46a_g \rightarrow 46a_u$	0.69437	494 (2.51)	0.0108	MLCT/ILCT
^1A_u	$45a_g \rightarrow 46a_u$	0.70433	477 (2.60)	0.0003	MLCT/ILCT
^1A_u	$44a_g \rightarrow 46a_u$	0.65475	386 (3.21)	0.2394	MLCT/ILCT
^1A_u	$46a_g \rightarrow 47a_u$	0.67110	358 (3.46)	0.1551	MLCT/ILCT
^1A_u	$44a_g \rightarrow 47a_u$	0.65402	312 (3.97)	0.0130	MLCT/ILCT
^1A_u	$43a_g \rightarrow 46a_u$	0.63092	285 (4.34)	0.1831	ILCT/MLCT
^1A_u	$45a_u \rightarrow 47a_g$	0.62311	267 (4.64)	0.3235	ILCT
^1A_u	$46a_g \rightarrow 48a_u$	0.44302	262 (4.72)	0.0169	MLCT/LLCT
	$46a_g \rightarrow 49a_u$	0.38396			MLCT/LLCT
^1A_u	$45a_g \rightarrow 50a_u$	0.58922	250 (4.95)	0.0084	MLCT/LLCT
	$45a_g \rightarrow 49a_u$	0.30858			MLCT/LLCT
^1A_u	$43a_g \rightarrow 47a_u$	0.64303	241 (5.13)	0.1179	ILCT
^1A_u	$44a_g \rightarrow 48a_u$	0.56091	235 (5.28)	0.0410	MLCT/LLCT
^1A_u	$45a_g \rightarrow 51a_u$	0.53269	230 (5.38)	0.1169	MLCT
	$46a_g \rightarrow 51a_u$	0.33235			MLCT

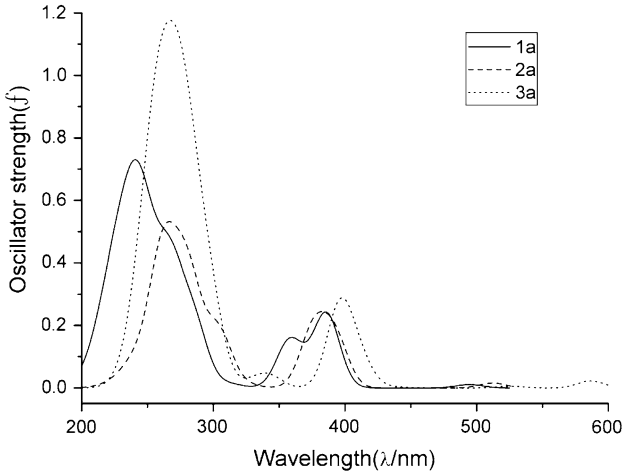

Fig. 3 Simulated absorption spectra of **1a**, **2a,** and **3a** in CH_2Cl_2 based on the TD-DFT/PCM calculations

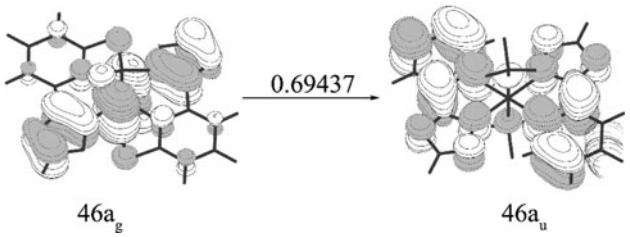

Fig. 4 Single-electron transitions with |CI coefficient| >0.2 in the TD-DFT calculations for the 494 nm absorption of **1a** in CH_2Cl_2

ILCT transition characters. In the meantime, the transition path of the lowest energy absorptions of **1b–2c** is similar to that of **1a** at 494 nm (see S-Tables 7–12). But the absorption of **3a** at 586 nm has different character. The only

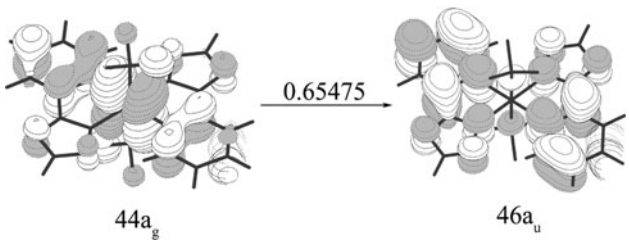

Fig. 5 Single-electron transitions with |CI coefficient| >0.2 in the TD-DFT calculations for the 386 nm absorption of **1a** in CH_2Cl_2

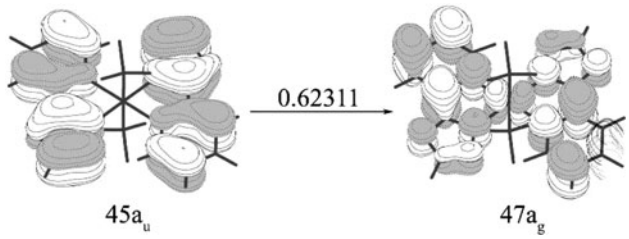

Fig. 6 Single-electron transitions with |CI coefficient| >0.2 in the TD-DFT calculations for the 267 nm absorption of **1a** in CH_2Cl_2

difference is the contributes of the metal composition of **3a** that originates from the d_{xz} and $d_{x^2-y^2}$; thus, the absorption of **3a** can be described as originating from the $[(d_{xz} + d_{x^2-y^2})Os + \pi(ppy)] \rightarrow [\pi^*(ppy)]$ excited state with different MLCT/ILCT character from those of **1a–2c**. By comparing the excitation energies of **1a**, **2a**, and **3a**, we found that the lowest-lying absorption is red-shifted from **1a** (494 nm) to **2a** (512 nm), and then to **3a** (586 nm), which is consistent with the increasing trend of the π-donating ability **1a** < **2a** < **3a**. In the same way, with

respect to **1a–c** and **2a–c** two series of complexes**,** we also found that with the increase in π electron-donating ability of R substituent in the order of **b** < **a** < **c**, the lowest energy absorption wavelengths are red-shifted, which is in accordance with the above analysis of frontier molecular orbital energy. These features are also familiar for Ir and Pt complexes [33–35].

Table 3 and S-Tables 7–12 also show that the most representative absorption of the second absorption band of **1a–3a** are between 382 and 397 nm. These absorptions are all attributed to the electronic transition from high occupied MOs (HOMO-HOMO-2) to low unoccupied MOs (LUMO or LUMO+1), with the similar oscillation intensity ($\sim$0.22), which is similar to the lowest energy absorption band in term of transition properties and intensity but is somewhat different from it in the relevant MO compositions of d(Os) and π(L).

Within the considered energy region, the highest energy absorption of **1a** appears at 267 nm. From Table 3, this absorption is originated from the transition of MO $45a_u \rightarrow$ MO $47a_g$, which have the largest oscillator strength of 0.3235. Also, MO $45a_u$ are dominantly localized on ptz ligand (98.6%), while MO $47a_g$ is contributed by π*(ptz) with the 91.2% composition. So, this excitations are dominantly assigned to a [π(ptz)] $\rightarrow$ [π*(ptz)] transition with pure ILCT transition characters. The intense absorption bands at 259, 280, 280, 268, 290, and 331 nm for **1b–3a** also can be described as a pure ILCT transition similar to **1a**, but with somewhat different π(L) and π*(L) component. By comparing **1–3a, 1a–c,** and **2a–c,** we found that these high-lying transitions have the similar variation trend as the lowest-lying absorption with the increase in the π-donating ability of the L ligand and the π electron-donating ability of R substituen. In addition, taking into account the highest-lying absorption, two laws can be drawn: (1) the pure ILCT type transitions are mainly originated from the transition of $a_u \rightarrow a_g$, and the transitions with other different characters are from $a_g \rightarrow a_u$ (see Table 3 and S-Tables 7–12); (2) the complexes **1b** and **2b** have the largest oscillation strength values compared with the **1a**, **1c**, and **2a**, **2c**, respectively (see S-Figs. 1, 2), which is different from the corresponding Ir(III) analogs [*trans*-$(C\hat{}N)_2Ir(PH_3)_2]^+$ [32]. To intuitively understand the absorption of these complexes, as examples, we display the electron density diagrams of **1a** in Figs. 4, 5, 6, in which three single-electron excitations corresponding to the maximal CI coefficients are involved.

3.3 Excited-state geometries and the emissions spectra in CH_2Cl_2 media

The main optimized geometry structural parameters of **1a–3a** in the ^3A_u excited states are given in S-Table 13. The calculated results show that the bond lengths, bond angles, and dihedral angles of the complexes in the excited state are slightly varied relative to those in the ground state. Take **1a** for example, the calculated Os–P (2.415 Å) and N1–N2 (1.398 Å) bond lengths in the excited state relax by ca. 0.068 and 0.023 Å, but the Os–N1 and Os–N2 bond lengths strengthen by 0.013 and 0.058 Å, respectively. The calculated bond angles and dihedral angles are slightly changed by 1.0–2.0°. The structure parameters of **1b–3a** have similar variation trend to that of **1a**. The slight changes of the geometry structural parameters result from the electron transfer from the metal Os(II) to the L ligand, which enhances the interaction between Os(II) atom and L ligand and weakens the interaction between Os(II) atom and PH_3 ligand upon excitation.

The calculated phosphorescence of **1a–3a** in CH_2Cl_2 media together with the measured values are given in Table 4; the frontier molecular orbital compositions responsible for the emissions are summarized in S-Table 14; The diagrams of the single-electron transitions related to the phosphorescence are shown in Fig. 7 and S-Fig. 3.

According to TD-DFT calculations, the lowest energy emissions of **1a–3a** were obtained at 660, 619, 698, 689, 616, 710, and 692 nm in CH_2Cl_2 solution, respectively, which agree well with the corresponding experimental values [14, 15] of **1b** (617 nm), **1c** (649 nm), and **2b** (617 nm). With respect to **1a**, Table 4 shows that the electronic transition of

Table 4 Calculated phosphorescent emissions of **1a–3a** using the TDDFTmethod, together with the corresponding experimental values

	States	Transition	|CI Coef.| >0.3	E, nm (ev)	Assignment	Exptl/nm[a]
1a	^3A_u	$46a_u \rightarrow 46a_g$	0.71645	660 (1.88)	^{3}MLCT/^{3}ILCT	
1b	^3A_u	$62a_u \rightarrow 62a_g$	0.71122	619 (2.00)	^{3}MLCT/^{3}ILCT	617
1c	^3A_u	$62a_u \rightarrow 62a_g$	0.71966	698 (1.78)	^{3}MLCT/^{3}ILCT	649
2a	^3A_u	$46a_u \rightarrow 46a_g$	0.71659	689 (1.80)	^{3}MLCT/^{3}ILCT	
2b	^3A_u	$62a_u \rightarrow 62a_g$	0.70995	616 (2.01)	^{3}MLCT/^{3}ILCT	617
2c	^3A_u	$62a_u \rightarrow 62a_g$	0.71718	710 (1.74)	^{3}MLCT/^{3}ILCT	
3a	^3A_u	$49a_u \rightarrow 49a_g$	0.70864	692 (1.79)	^{3}MLCT/^{3}ILCT	

[a] From Refs. [14, 15]

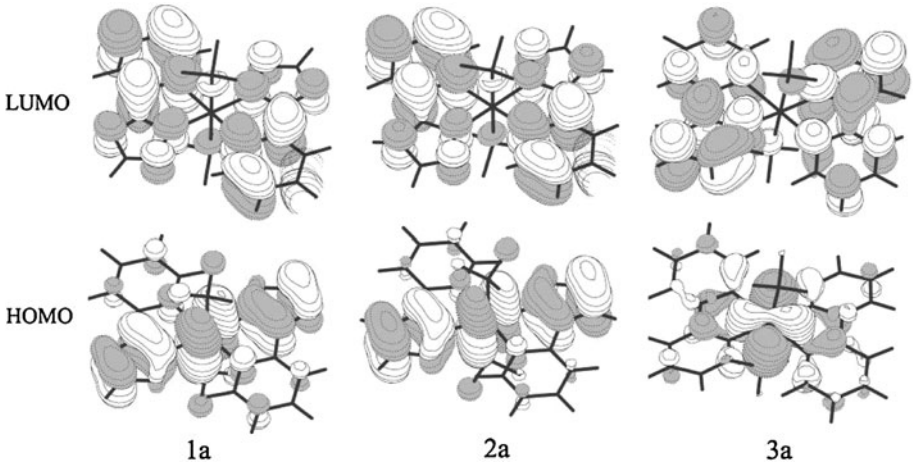

Fig. 7 Electron density diagrams of HOMO and LUMO for **1a**, **2a**, and **3a** from UB3LYP calculations

MO $46a_u \rightarrow$ MO $46a_g$ contributes to the emission at 660 nm. S-Table 14 shows that MO $46a_u$ is contributed by 91.4% π^*(ptz) component, while MO $46a_g$ is composed of 58.5% $(d_{xy} + d_{yz})$Os and 37.7% π(ptz). Thus, the emission at 660 nm of **1a** originates from the $^3\{[(d_{xy} + d_{yz})$ Os $+ \pi$(ptz)] $[\pi^*$(ptz)]$\}$ excited state with ^{3}MLCT/^{3}ILCT character. The calculated phosphorescent of **1b–2c** has similar character to that of **1a** (see Table 4; S-Table 14). But the emission of **3a** at 692 nm has different ^{3}MLCT/^{3}ILCT characters. The excitation of MO $49a_u \rightarrow$ MO $49a_g$ is responsible for the emission at 692 nm. S-Table 14 shows that MO $49a_g$ has 74.5% $(d_{xz} + d_{x^2-y^2})$Os and 24.6% π(ppy), while MO $49a_u$ is dominantly localized on the ppy ligand. Thus, the emission of **3a** at 692 nm can be described as originating from the $^3\{[(d_{xz} + d_{x^2-y^2})$Os $+ \pi$(ppy)] $[\pi^*$(ppy)]$\}$ excited state. When compared the emission of **1a**, **2a**, and **3a**, results indicate that with the increase in the π-conjugation effect of the L ligand in the order **1a** < **2a** < **3a**, the emission has a red-shift from 660 (**1a**) to 689 (**2a**) and then to 692 nm (**3a**). By comparing **1a–c** with **2a–c,** we found that with the increase in the π electron-donating ability of R substituent, the emission wavelengths are also red-shifted. As in previous investigations, many researchers have got the similar conclusion [32–35].

Obviously, the phosphorescent excited state is relevant to both the metal and the ligands, and the intense interaction between the metal and the ligands in the frontier molecular orbitals leads to the spin-forbidden LC ($\pi\pi^*$) transition. The calculated metal compositions in the HOMOs of **1b**, **1c**, and **2b** are 65.1, 55.4, and 61.5%, respectively, while their respective measured quantum efficiencies are 0.62, 0.25, and 0.50 [14, 15], which show the same trend in both the metal composition and quantum efficiency in the order of **1c** < **2b** < **1b**. We can presume that the more metal components in the frontier molecular orbital, the more possible can make the spin-forbidden transition. This law was also found in that of a series of iridium(III) complexes $Ir(C\hat{}N)_2LX$ in our previous investigations [35], and it could be a guidance to design new phosphorescent material. But, it is only suitable to the complexes with the lowest energy absorptions and emissions mainly from the MLCT transition [36].

4 Conclusions

To provide insight into the properties of their ground and excited states, detailed calculations on seven novel $[Os(LR)_2(PH_3)_2]$ (L = ptz, ppz, or ppy; R = H, CF_3, or t-Bu) complexes were performed with the density functional theory methods and the PCM solvent model. The calculated results reveal that the higher-energy occupied molecular orbitals are composed of d(Os) and π(L), while the lower energy unoccupied molecular orbitals are dominantly localized on the L ligand. The lowest energy absorptions in the UV–visible region are assigned to a $[d(Os) + \pi(L)] \rightarrow [\pi^*(L)]$ MLCT/ILCT transition. The phosphorescence can be described as originated from a $^3\{[[d(Os) + \pi(L)]$ $[\pi^*(L)]\}$ excited state with ^{3}MLCT/^{3}ILCT character.

According to our research, we found that the metal composition in the higher-energy occupied orbitals can be adjusted by tuning the electron-donating ability of the R substituents and π-conjugation ability of the L ligands. The large metal compositions in the frontier molecular orbitals can bring about high quantum efficiency. Furthermore, the MLCT transition is present in all UV–visible regions along with the LC (ligand-centered) transition, and this is the decisive factor for the spin-forbidden electron transition to occur. This law was also found in a series of iridium(III) complexes $Ir(C\hat{}N)_2LX$ in our previous investigations [34], which are very practical to design highly efficient phosphorescent materials.

Acknowledgments This work is supported by the Natural Science Foundation of China (Grant Nos. 20573042, 20333050, and 20173021) and the Foundation of State Key Laboratory of Theoretical and Computational Chemistry.

References

1. Demadis KD, Hartshorn CM, Meyer TJ (2001) Chem Rev 101:2655
2. Carlson B, Phelan GD, Kaminsky W, Dalton L, Jiang X, Liu S, Jen AKY (2002) J Am Chem Soc 124:14162
3. Xin H, Li F, Shi M, Bian ZQ, Huang HC (2003) J Am Chem Soc 125:7166
4. Lo KKW, Chung CKT, Lee KM, Lui LH, Tsang KHK, Zhu NY (2003) Inorg Chem 42:6886
5. Hamilton JG, Rooney JJ, DeSimone JM, Mistele C (1998) Macromolecules 31:4387
6. Gassner F, Dinjus E, Gorls H, Leitner W (1996) Organometallics 15:2078
7. Haynes A, Maitlis PM, Morris GE, Sunley GJ, Adams H, Badger PW, Bowers CM, Cook DB, Elliott PIP, Ghaffar T, Green H, Griffin TR, Payne M, Pearson JM, Taylor MJ, Vickers PW, Watt RJ (2004) J Am Chem Soc 126:2847
8. Kawamura Y, Goushi K, Brooks J, Brown JJ, Sasabe H, Adachi C (2005) Appl Phys Lett 86:1104
9. Baldo MA, Thompson ME, Forrest SR (1999) Pure Appl Chem 71:2095
10. Yang QZ, Wu LZ, Wu ZX, Zhang LP, Tung CH (2002) Inorg Chem 41:5653
11. Balzani V, Barigelletti F, De Cola L (1990) Top Curr Chem 158:31
12. Craig DC, Scudder ML, McHale WA, Goodwin HA (1998) Aust J Chem 51:1131
13. Chen YL, Sinha C, Chen IC, Liu KL, Chi Y, Yu JK, Chou PT, Lu TH (2003) Chem Commun 3046
14. Chou PT, Chi Y (2007) Chem Eur J 13:380
15. Chou PT, Chi Y (2006) Eur J Inorg Chem 3319
16. Kappaun S, Sax S, Eder S, Moller KC, Waich K, Niedermair F, Saf R, Mereiter K, Jacob J, Mullen K, List EJW, Slugovc C (2007) Chem Mater 19:1209
17. Wu FI, Shih PI, Shu CF, Tung YL, Chi Y (2005) Macromolecules 38:9028
18. Statmann RE, Scuseria GE (1998) J Chem Phys 109:8218
19. Paul F, Costa G, Bondon A, Gauthier N, Sinbandhit S, Toupet L, Costuas K, Halet JF, Lapinte C (2007) Organometallics 26:874
20. O'Grady E, Kaltsoyannis N (2004) Phys Chem Chem Phys 6:680
21. Pan QJ, Zhang HX (2004) Organometallics 23:5198
22. Pan QJ, Fu HG, Yu HT, Zhang HX (2006) Inorg Chem 45:8729
23. PyykkÖ P (2004) Angew Chem Int Ed 43:4412
24. Bryce AB, Charnochk JM, Pattrichk RAD, Lennie AR (2003) J Phys Chem A 107:2516
25. Nemykin VN, Makarova EA, Grosland JO, Hadt RG, Koposov AY (2007) Inorg Chem 46:9591
26. Becke AD (1987) Phys ReV A 38:3098
27. Casida ME, Jamorski C, Casida KC, Salahub DR (1998) J Chem Phys 108:4439
28. Cossi M, Scalmani G, Regar N, Barone V (2002) J Chem Phys 117:43
29. Hay PJ, Wadt WR (1985) J Chem Phys 82:299
30. Frisch MJ, Trucks GW, Schlegel HB, Scuseria GE, Robb MA, Cheeseman JR, Montgomery JA Jr, Vreven T, Kudin KN, Burant JC, Millam JM, Iyengar SS, Tomasi J, Barone V, Mennucci B, Cossi M, Scalmani G, Rega N, Petersson GA, Nakatsuji H, Hada M, Ehara M, Toyota K, Fukuda R, Hasegawa J, Shida M, Nakajima T, Honda Y, Kitao O, Nakai H, Klene M, Li X, Knox JE, Hratchian HP, Cross JB, Bakken V, Adamo C, Jaramillo J, Gomperts R, Stratmann RE, Yazyev O, Austin AJ, Cammi R, Pomelli C, Ochterski JW, Ayala PY, Morokuma K, Voth GA, Salvador P, Dannenberg JJ, Zakrzewski VG, Dapprich S, Daniels AD, Strain MC, Farkas O, Malick DK, Rabuck AD, Raghavachari K, Foresman JB, Ortiz JV, Cui Q, Baboul AG, Clifford S, Cioslowski J, Stefanov BB, Liu G, Liashenko A, Piskorz P, Komaromi I, Martin RL, Fox DJ, Keith T, Al-Laham MA, Peng CY, Nanayakkara A, Challacombe M, Gill PMW, Johnson B, Chen W, Wong MW, Gonzalez C, Pople JA (2004) Gaussian 03, revision C.02. Wallingford, Gaussian, Inc
31. Che CM, Lai TF, Chung WC, Schaefer WP, Gray HB (1987) Inorg Chem 26:3907
32. Liu T, Zhang HX, Xia BH (2007) J Phys Chem A 111:8724
33. Zhang JP, Zhou X, Liu T, Bai FQ, Zhang HX, Tang AQ (2008) Theor Chem Acc 121:123
34. Liu T, Xia BH, Zhou X, Zhang HX, Pan QJ, Gao JS (2007) Organometallics 26:143
35. Zhou X, Zhang HX, Pan QJ, Xia BH, Tang AQ (2007) J Phys Chem A 109:8809
36. Zhang JP, Zhou X, Bai FQ, Zhang HX, Tang AQ (2009) Theor Chem Account 122:31